*Journal of Advanced Ceramics*
2019, **8**(2): 0–0
https://doi.org/10.1007/s40145-019-0314-8
ISSN 2226-4108
CN 10-1154/TQ

**Research Article**

# Effect of the sintering technique on the ferroelectric and $d_{33}$ piezoelectric coefficients of $Bi_{0.5}(Na_{0.84}K_{0.16})_{0.5}TiO_3$ ceramic

G. HERNANDEZ-CUEVAS[a], J. R. LEYVA MENDOZA[a], P. E. GARCÍA-CASILLAS[a], C. A. RODRÍGUEZ GONZÁLEZ[a], J. F. HERNANDEZ-PAZ[a], G. HERRERA-PÉREZ[b], L. FUENTES-COBAS[b], S. DÍAZ DE LA TORRE[c], O. RAYMOND-HERRERA[d], H. CAMACHO-MONTES[a,*]

[a]*Instituto de Ingeniería y Tecnología*, *Universidad Autónoma de Ciudad Juárez*, *Av. Del Charro 450 Norte Cd. Juárez*, *Chihuahua*, *32310*, *México*
[b]*Centro de Investigación en Materiales Avanzados*, *Miguel de Cervantes 120*, *Chihuahua 31109*, *Chihuahua*, *México*
[c]*Centro de Investigación e Innovación Tecnológica*, *Instituto Politécnico Nacional*, *Cerrada de Cecati s/n*, *Azcapotzalco*, *Santa Catarina*, *02250*, *Ciudad de México*, *México*
[d]*Centro de Nanociencias y Nanotecnología*, *Universidad Nacional Autónoma de México*, *Km. 107 Carretera Tijuana-Ensenada*, *AP. 14*, *Ensenada 22860*, *Baja California*, *México*

Received: September 24, 2018; Revised: December 13, 2018; Accepted: January 3, 2019


**Abstract:** In the search of lead-free piezoelectric materials, ceramic processing techniques offer potential tools to increase the piezoelectric and ferroelectric properties in addition to new chemical compositions. Powders of pure BNKT16 ($Bi_{0.5}(Na_{0.84}K_{0.16})_{0.5}TiO_3$) phase were synthesized by sol–gel method with a low crystallization temperature (750 ℃). Ceramic samples were sintered by pressureless sintering (PLS), sinter-forging (SF), and spark plasma sintering (SPS) techniques. Structural, morphological, and chemical characterizations were performed by XRD, Raman, EDS, and SEM. Sintered samples by PLS and SF exhibit rod-like grains associated to bismuth volatility. The highest remanent polarization (11.05 μC/cm$^2$), coercive field (26.2 kV/mm), and piezoelectric coefficient (165 pC/N) were obtained for SF sample. The piezoresponse force microscopy (PFM) analysis shows that the crystallites at the nanoscale exhibit piezoelectric phenomenon and the highest piezoelectric response is reported for PLS sample. The presence of the rhombohedral phase, the increase in grain and crystallite size, and the oriented rod-like inclusions favoring the crystallographic texture are facts that enhance the piezoelectric coefficient for BNKT16 piezoceramics.

**Keywords:** lead-free piezoelectrics; sol–gel; pressureless sintering (PLS); sinter-forging (SF); spark plasma sintering (SPS); piezoresponse

* Corresponding author.
E-mail: hcamacho@uacj.mx

## 1 Introduction

The production of piezoelectric materials rapidly developed in the late 1950s due to the number of discovered piezoelectric ceramics, for example, the lead niobate and lead zirconate titanate (PZT) piezoelectric ceramics [1]. The PZT with high electromechanical coupling factor implies a high level of production with contaminants in the form of lead oxide (PbO) or lead zirconate titanate. This mainly occurs during calcination and sintering, where the PbO evaporates. As a consequence, in 2003 the European Union included PZT ceramics in the legislature as a toxic substance that needs to be replaced by safer materials [2]. Lead-free piezoelectric ceramics exhibit superior electromechanical responses near the morphotropic phase boundary (MPB). It is reported that their high piezoelectric response is due to the phase coexistence of rhombohedral and tetragonal phases at the optimal composition, i.e., the MPB [3–7].

NBT-based ceramics is a very intense field of research looking for lead-free piezoelectric ceramics [8,9]. Among them, the systems $Bi_{0.5}Na_{0.5}TiO_3$ (BNT) and $Bi_{0.5}K_{0.5}TiO_3$ (BKT), are two examples that have received considerable attention due to their excellent ferroelectric and piezoelectric properties near their rhombohedral–tetragonal composition (MPB) [5,10]. Bismuth sodium potassium titanate (BNKT) has been synthesized by sol–gel showing excellent dielectric, piezoelectric, and ferroelectric properties [5]. The synthesis of BNKT by chemical methods such as sol–gel has shown to be more effective because it is performed at a lower temperature than the solid-state reaction method, the microstructure is most homogeneous, and a better morphology control is achieved. Increasing grain size translates into excellent dielectric and piezoelectric properties [11]. The sinter-forging technique in ceramic materials induces a crystallographic texture with a preferred orientation [12]. The textured bismuth titanate (BiT) has better electrical properties along axis, i.e., in the direction of the preferred orientation [13]. Spark plasma sintering (SPS) allows very fast heating rates, very short holding time, and the possibility to obtain high dense samples at lower temperatures than the most sintering techniques [14]. Therefore, it is expected that the application of SPS technique in BNKT ceramics could suppress the volatilization of Bi during sintering [15,16]. In the present study, the synthesis of $0.84(Bi_{0.5}Na_{0.5}TiO_3)$–$0.16(Bi_{0.5}K_{0.5}TiO_3)$ (BNKT16) was done using the sol–gel technique. The attention is focused on the effects of the pressureless sintering (PLS), sinter-forging (SF), and spark plasma sintering (SPS) techniques on structural and electrical properties.

## 2 Experimental procedures

The precursors used in the present work were analytical grade bismuth nitrate pentahydrate ($Bi(NO_3)_3{\cdot}5H_2O$) (Alfa Aesar 98%, USA), potassium nitrate ($KNO_3$) (Alfa Aesar 99%, USA), sodium nitrate ($NaNO_3$) (Alfa Aesar 99%, USA), and tetrabutyl titanate ($Ti(OC_4H_9)_4$) (Alfa Aesar 99%, USA). Acetic acid ($CH_3COOH$) (J. T. Baker 99%, USA), distilled water, and ethanol ($CH_3CH_2OH$) (Alfa Aesar 99%, USA) were used as solvents. Bismuth nitrate pentahydrate was dissolved in acetic acid (1:5 *v*/*v*). Sodium nitrate and potassium nitrate were dissolved in distilled water (1:20 *v*/*v*). The mixture was then introduced into a prepared solution of tetrabutyl titanate in ethanol (1:50 *v*/*v*). Stirring was maintained until clear solutions were obtained. Then, all the solutions were mixed and stirred for 2 h, and a homogeneous sol was obtained. The sol was then heated at 70 ℃ under continuous stirring for 24 h to get a dry gel. A second drying step at 400 ℃ for 4 h was performed. The resulting powders were calcined at 750 ℃ for 4 h followed by 6 h with 80% weight of 0.5 mm zirconium ball milling process to break agglomerates.

For PLS green sample preparation, the BNKT powders were pulverized with a mortar and pestle adding 3 wt% aqueous polyvinyl alcohol (PVA) and pressed into pellets with a diameter of 6 mm under a uniaxial force of 6 kN. Sintering of the green body was performed at 1150 ℃ for 3 h in a Carbolite VST 1700 furnace. Bismuth volatilization restricts the range to select an effective sintering temperature. For a lower temperature, sintering is not effective enough and, for a higher one, bismuth volatilization is too high [5,17]. In general, the effect of volatile elements for lead-free piezoelectric ceramics is an issue of interest [18]. In the case of SF sample, the green body was placed between two platinum plates to prevent the sample reaction with the alumina pistons. After conventional firing (1150 ℃) for 1 h, the uniaxial stress was gradually applied at a 10 N/min rate until reaching a constant value of 7073.55 Pa (200 N). It was held for

1 h. Pressing was performed with an Instron 5967 tester system coupled to the furnace. Then, the applied stress was released and the 1150 ℃ temperature was held for 1 h annealing. The SPS process was carried out applying 500 A, pulse switch on/off 12/2, and 4 kN load on a 10 mm diameter graphite die in a Dr. Sinter facility. The densities were estimated using the Archimedes' method (ASTM C373).

The X-ray diffraction (XRD) patterns of the heat-treated samples were recorded on a PANalytical X'pert PRO powder X-ray diffractometer equipped with an X′Celerator detector. A monochromatic X-ray source of Cu Kα radiation ($\lambda \approx 1.5406$ Å) was used with 40 kV/30 mA of power. The XRD patterns were collected in the range of 10°–100° using the step-scanning mode with a step of 0.017° in $2\theta$ and 60 s of step counting time. For the SPS sample, lattice parameters and the atomic positions were determined from the XRD patterns by the Rietveld refinement method using the FullProf Suite (version 2017) software package [19]. For the refinement, the following parameters were considered: (i) scale factor; (ii) zero displacement correction; (iii) unit cell and background parameters; (iv) peak profile parameters (full width at half maximum, FWHM and shape parameters), using a pseudo-Voigt function including the peak asymmetry.

The crystallite size was estimated by Scherrer's equation. For the morphological characterization, BNKT16 ceramics were sliced transversally, polished, and thermally etched at 1050 ℃ for 1 h. Then, they were analyzed by scanning electron microscopy (SEM) in a Hitachi SU 5000 equipped with energy dispersive spectroscopy (EDS), and the average of the grain size was estimated from SEM micrographs by an image-processing analyzing program (ImageJ 1.50i, National Institutes of Health, USA). Raman spectrums were performed with a WITec Focus Innovation.

Hysteresis loops were obtained using a Radian Technologies Precision Workstation (model P-WS) and high-power amplifier TREK (model 609A, Albuquerque, New Mexico, USA), with an applied electric field of 70 kV/cm over the pellets. Samples were polarized in a silicone oil bath at room temperature by applying a DC field of 40 kV/cm for 30 min. The piezoelectric constant $d_{33}$ was measured using a piezo $d_{33}$ meter (Pennebaker model 8000). The local piezoresponse was examined using switching spectroscopy piezo-response force microscopy (SS-PFM) using an AFM system (MFP-3D, Asylum Research, Oxford Instruments). Details of the SS-PFM experimental procedure can be found elsewhere [20].

## 3 Results and discussion

### 3.1 X-ray diffraction

Figure 1 shows the XRD pattern for the BNKT16 powders obtained by sol–gel. The XRD pattern is associated to the heat-treated powders obtained at 750 ℃. It suggests a perovskite structure with a single pseudo-cubic phase. It is known that the A sites are occupied by Bi, Na, and K [1].

Figure 2 shows the XRD patterns and the Rietveld refinement results for the BNKT16 SPS, PLS, and SF samples where the coexistence of tetragonal and rhombohedral phases of the BNKT, labeled as "t" and "r" respectively is seen. Herein, for the Rietveld refinement, the coexistence of the rhombohedral and tetragonal phases is considered as it was previously reported by Kreisel *et al.* [21]. Table 1 summarizes the lattice parameters, the phase volume fraction obtained from Rietveld refinement process for the compositions obtained by the three different sintering techniques, and each global $\chi^2$ adjustment quality parameter. Table 2 reports the atom normalized coordinates, occupancy, and the Wyckoff positions for each spatial group. The atomic positions for the tetragonal phase with *P*4*mm* spatial group were refined for the SPS sample, and the atomic positions for the tetragonal *P*4*bm* and rhombohedral *R*3*c* phases were refined for the PLS sample. The BNKT16-*R*3*c* is also present for SPS and SF, BNKT16-*P*4*bm* for SF. However, it is not necessary to refine the atomic position again, because no improvement is obtained for $\chi^2$ adjustment parameter.

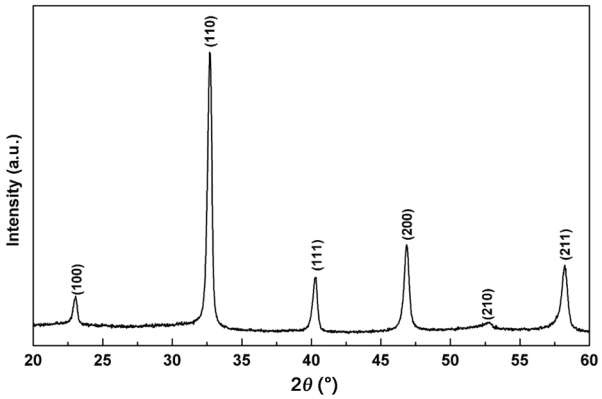


**Fig. 1** XRD pattern for the BNKT16 powders obtained by sol–gel.

**Table 1 X-ray crystallographic data, the Rietveld adjusted lattice parameter, and phase fraction for $Bi_{0.5}(Na_{0.84}K_{0.16})_{0.5}TiO_3$**

| Rietveld parameter | Tetragonal phase | Quasic cubic tetragonal phase | Rhombohedral phase |
|---|---|---|---|
| Space group | *P4mm* (No. 99) | *P4bm* (No. 100) | *R3c* (No. 167) |
| Point group | $C_{4v}$ (4 mm) | $C_{4v}$ (4 mm) | $C_{4v}$ (4 mm) |
| SPS: *a* (Å), *b* (Å), *c* (Å) | 3.894(6), 3.894(6), 3.951(7) | | 5.511(11), 5.511(11), 13.527(41) |
| PLS: *a* (Å), *b* (Å), *c* (Å) | | 5.56(3), 5.56(3), 3.90(1) | 5.493(1), 5.493(1), 13.569(6) |
| SF: *a* (Å), *b* (Å), *c* (Å) | | 5.706(105), 5.706(105), 3.959(17) | 5.497(3), 5.497(3), 13.594(9) |
| SPS frac (%) | 97.44 | 0 | 2.56 |
| PLS frac (%) | 0 | 14.41 | 85.59 |
| SF frac (%) | 17.80 | 2.48 | 97.52 |
| SPS $\chi^2$ | | 2.28 | |
| PLS $\chi^2$ | | 1.380 | |
| SF $\chi^2$ | | 2.25 | |

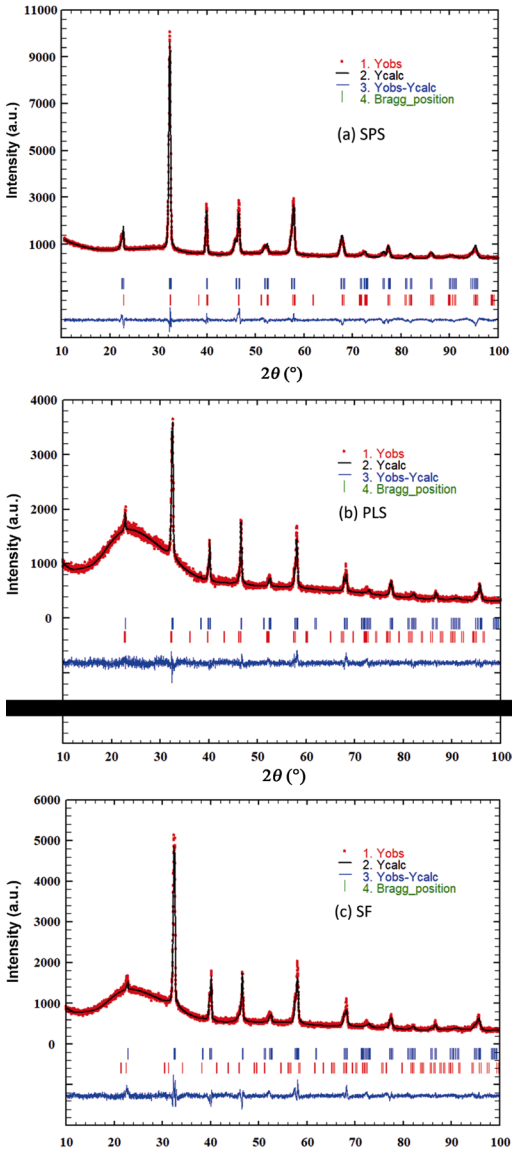


**Fig. 2** Rietveld refinement for the BNKT16 PLS, SF, and SPS samples.

**Table 2 Chemical element, occupancy, Wyckoff position, and the atom normalized coordinates for BNKT16 with the spatial groups *P4mm*, *P4bm*, and *R3c***

| Spatial group | Chemical element | Occupancy | Wyckoff position | Atom normalized coordinate | | |
|---|---|---|---|---|---|---|
| | | | | *x* | *y* | *z* |
| *P4mm* | Na | 0.34 | 1a | 0.0000 | 0.0000 | –0.0472 |
| | K | 0.16 | 1a | 0.0000 | 0.0000 | –0.0472 |
| | Bi | 0.50 | 1a | 0.0000 | 0.0000 | –0.0472 |
| | Ti | 1.00 | 1b | 0.5000 | 0.5000 | 0.5000 |
| | O | 1.00 | 1b | 0.5000 | 0.5000 | 0.0102 |
| | O | 2.00 | 2c | 0.5000 | 0.0000 | 0.5273 |
| *P4bm* | Na | 0.34 | 2b | 0.5000 | 0.0000 | 0.5530 |
| | K | 0.16 | 2b | 0.5000 | 0.0000 | 0.5530 |
| | Bi | 0.50 | 2b | 0.5000 | 0.0000 | 0.5530 |
| | Ti | 1.00 | 2a | 0.0000 | 0.0000 | 0.0110 |
| | O | 1.00 | 2a | 0.0000 | 0.0000 | 0.5120 |
| | O | 2.00 | 8d | 0.7630 | 0.2630 | 0.0300 |
| *R3c* | Na | 0.34 | 6a | 0.0000 | 0.0000 | 0.2627 |
| | K | 0.16 | 6a | 0.0000 | 0.0000 | 0.2627 |
| | Bi | 0.50 | 6a | 0.0000 | 0.0000 | 0.2627 |
| | Ti | 1.00 | 6a | 0.0000 | 0.0000 | 0.5100 |
| | O | 3.00 | 18a | 0.1260 | 0.3360 | 0.0833 |

For the SPS sample, the split peak at $2\theta \approx 46°$ and the unique peak at $2\theta \approx 40°$ can be observed as evidence of the tetragonal BNKT phase $((001)_T$ and $(100)_T$ peaks, *P4mm* space group, $C_{4v}$, Fig. S1(a) in the Electronic Supplementary Material (ESM)) [22]. The other way around (unique peak for $2\theta \approx 46°$ and split peak for $2\theta \approx 40°$) is a sign of the BNKT rhombohedral phase $((006)_R$ and $(202)_R$ peaks, Fig. S1(c) in the ESM). For the SPS sample, the preponderant phase is the tetragonal (97.44%) as can

be observed in Fig. 2(a) and reported in Table 1. For the sample obtained by the conventional PLS method, it can be noticed that the split peaks are located between 39° and 41°, which suggests the presence of a rhombohedral phase with a *R*3*c* space group ($C_{3v}$, Fig. S1(c) in the ESM) as can be expected for this composition [23]. The Rietveld adjustment suggests that the rhombohedral is the preponderant phase with a concentration of 85.59% (Table 1). The XRD pattern for the sample obtained by SF method maintains the same split peaks for $39° < 2\theta < 41°$. It can also be pointed out that these split peaks are better defined for SF than for PLS. It seems that split peaks are also present for $22° < 2\theta < 24°$, which may suggest the presence of the tetragonal phase. Therefore, the coexistence of rhombohedral and tetragonal phases [24] can be expected. In fact, the Rietveld adjustment is reporting the coexistence of tetragonal (2.48%) and rhombohedral (97.52%) phases. As can be noticed, the rhombohedral fraction increases in the following sequence: SPS, PLS, and SF. For the PLS and SF samples, the best adjustment is obtained considering the space group *P*4*bm* instead of *P*4*mm*, which also corresponds to the tetragonal crystal system.

### 3. 2 Raman spectroscopy

Figure 3 shows the Raman spectra analysis of the BNKT16 powders and the sintered samples obtained by PLS, SF, and SPS methods. Raman analysis for all samples considered the criterion of Gaussian peak fitting. Table 3 reports the wave number of each Raman fitted peak shown in Fig. 3 and its relative intensity. The Raman active modes can be estimated with the help of the Bilbao crystallographic server [25,26]. The presence of 12 active modes are predicted for the BNKT tetragonal phase *P*4*mm*, $\Gamma_{Raman} = 5A_1 + B_1 + 6E$ ((S.3) in the ESM); 31 active modes for the BNKT tetragonal phase *P*4*bm*, $\Gamma_{Raman} = 7A_1 + 3B_1 + 6B_2 + 15E$ ((S.6) in the ESM); and 19 active modes for the BNKT rhombohedral *R*3*c*, $\Gamma_{Raman} = 6A_1 + 13E$ ((S.9) in the ESM).

Then, four regions can be described in the Raman spectra, which are: 100–180, 180–430, 430–680, and 680–930 $cm^{-1}$ [25]. The first band region, in the range of 100–180 $cm^{-1}$ describes the A-site vibrations associated to the Bi–O, Na–O, and K–O bonds which is dominated by an intense band centered at 125 $cm^{-1}$ assigned to a Raman active mode $A_1$. According to Kreisel *et al*. [21], who studied a similar composition BNT–BKT, the Raman shift observed in this band is sensitive to the pressure conditions and by another type of cation substitution. Almost no difference can be observed between the powder sample and the sintered ones. The second region is located in the range of 180–430 $cm^{-1}$ and is attributed to the vibration of the Ti–O bond. The peak centered at 265 $cm^{-1}$ (Raman active mode $A_1$) is associated to the tetragonal phase in the perovskite structure. Deconvolution shows one peak for the powder sample and two peaks for the

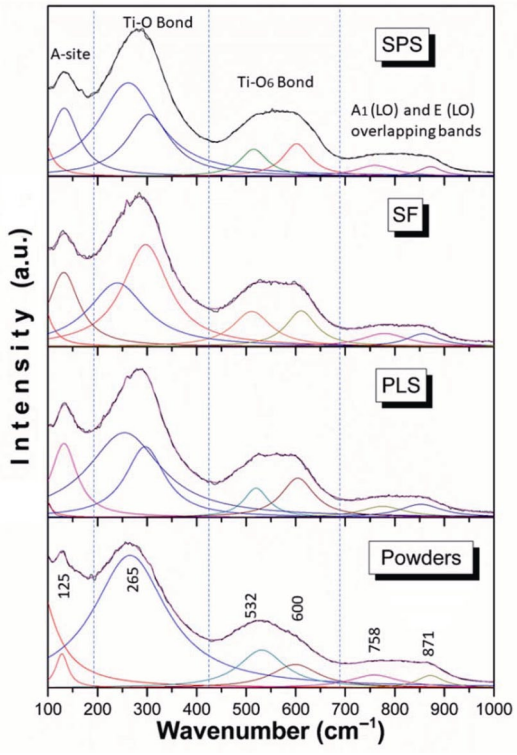


**Fig. 3** Raman spectra of BNKT16 powders, and sintered samples by PLS, SF, and SPS.

**Table 3 Raman shift wave number and relative intensity for the BNKT16 powders, and sintered samples by PLS, SF, and SPS**

| Wave number ($cm^{-1}$) / Relative intensity | A-site | Ti–O bond | | Ti–$O_6$ bond | | $A_1$(LO) and E(LO) | |
|---|---|---|---|---|---|---|---|
| Powders | 125 | 255 | | 532 | 600 | 758 | 871 |
| | 0.26 | **1.00** | | 0.28 | 0.18 | 0.10 | 0.09 |
| PLS | 130 | 256 | 293 | 518 | 605 | 774 | 852 |
| | 0.87 | **1.00** | 0.84 | 0.34 | 0.46 | 0.13 | 0.15 |
| SF | 130 | 238 | 287 | 521 | 608 | 771 | 853 |
| | 0.67 | 0.73 | **1.00** | 0.26 | 0.29 | 0.10 | 0.11 |
| SPS | 130 | 265 | 302 | 558 | 602 | 758 | 871 |
| | 0.73 | **1.00** | 0.66 | 0.34 | 0.35 | 0.12 | 0.13 |

sintered ones. It can also be observed in Table 3 that peak shift wave number is sensitive to the sintered technique. It means that in all samples, there is a coexistence of tetragonal phase with rhombohedral phase as it was discussed in the XRD section.

The third region, located between 430 and 680 $cm^{-1}$, is attributed to the oxygen displacements and is interpreted in terms of the polyhedral $TiO_6$ vibrations [21]. The peak at 532 $cm^{-1}$ for the powder sample shifts to values that run from 510 to 558 $cm^{-1}$, then this peak turns out to be sensitive to the sintered technique. The broad band observed in the fourth region could be assigned to the $A_1$(LO) and E(LO) overlapping bands [27]. The peak analysis interpretation for the PLS sample suggests an important contribution of the rhombohedral phase over the tetragonal phase. The spectral shape of the SF sample shows a peak broadening in the second region that could be attributed to a splitting into two Raman bands that are associated to an important presence of a tetragonal phase as discussed in the XRD section. According to previous reports [28,29], other Raman bands appear when a tetragonal symmetry is more evident as noticed in the XRD patterns for the PLS and SPS methods. The SPS spectral shape shows a broadened peak in the second region. This can be interpreted like an important contribution from a tetragonal phase. The variation of the Raman spectrum shape for this compound obtained by different processes is a clear demonstration of changes in the contribution of rhombohedral and tetragonal symmetry in the structure. In the region of 680–930 $cm^{-1}$, the presence of broader peaks is related to the oxygen vacancy presence [27].

### 3. 3 Scanning electron microscopy and energy dispersive spectrometer

Figure 4 shows the secondary electron-SEM micrographs of the BNKT16 sintered by (a) PLS, (b) SF, and (c) SPS, and their respective grain size distribution. Only nearly spherical grains were considered for the grain size determination. The BNKT16 samples sintered by PLS and SF show grains with two well-differentiated morphologies: nearly spherical grains commonly seen in most ceramics, and the rod-like grains which can be associated with the rhombohedral phase. Average grain sizes of 1.81 and 1.89 μm were obtained for PLS and SF samples, respectively. The SPS sample shows a lower average grain size of 1.76 μm and it does not exhibit rod-like grains. This can be explained by the short time needed to accomplish the sintering process, thus reducing the volatilization of alkaline elements and in consequence inhibiting the formation of the rod-like grains which did not have sufficient time to form. Rod-like grains are generally larger than spherical ones and they are more frequently seen in SF sample.

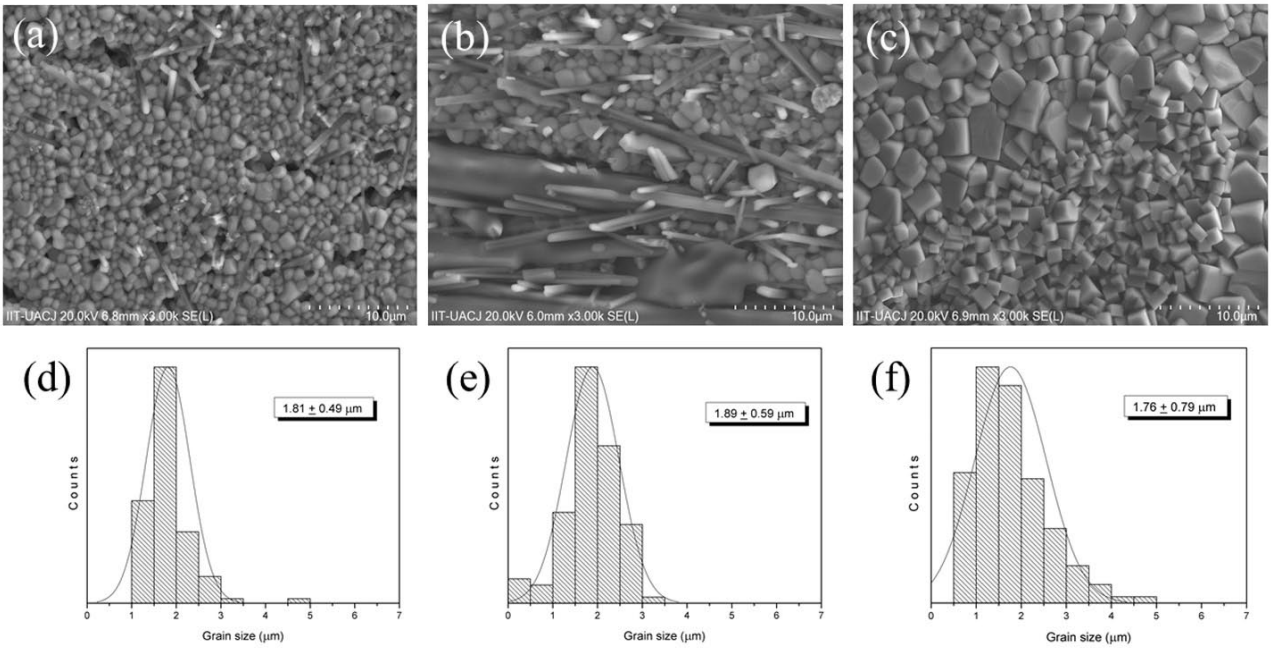


**Fig. 4** SEM micrographs of thermally etched surfaces of the BNKT16 ceramics sintered by (a) PLS, (b) SF, and (c) SPS.

The Na/K ratio is very important for the piezoelectric response in the BNKT systems [30,31]. To obtain the semi-quantitative Na/K ratios and atomic percentage, energy dispersive spectroscopy (EDS Bruker 60) analysis was done in all BNKT16 samples manufactured by different processes. Figure 5 illustrates the BSE–SEM images for the microstructure regions of the BNKT16 (a) PLS, (b) SF, and (c) SPS ceramics. The grain matrix (marked regions as a.2, b.1, and c.1) has a nominal composition ratio Na/K ratio 9.41, 1.21, and 2.8 for PLS, SF, and SPS samples, respectively. This nominal ratio is higher in the matrix when the powders are sintered by PLS, and is lower when the powders are sintered by SF. Table 4 summarizes the EDS results for all samples; the table clearly reveals that the element concentration is highly affected by the used sintering technique. A clear tendency related to Bi volatilization can be clearly observed. In the rods, lower atomic percentage of Bi is detected, while the atomic percentage of K exhibits higher values than those detected in the grain matrix. Hence, considering rod composition (marked as regions a.1 and b.2 in Fig. 5), a question arises about whether a secondary phase is formed or not, because of the high degree of Bi volatilization. From the XRD patterns (Fig. 2), no secondary phase is detected. It is worthy to mention that BNKT rod-like grains have been previously reported only by two other research works [3,30] and they have considered the rods as a secondary phase based on local Raman measurements. At higher temperature, they also visualized the secondary phase by XRD.

In summary, evidence of phase coexistence can be observed by means of XRD and Raman analysis. Rod-like grains can be considered as a secondary phase in the sense that they have a remarkable difference in the Bi composition. However, evidence of a different crystal structure is not detectable. Henceforth, local properties at this level can be different in comparison to nearly circular grains.

**Table 4 Composition of the regions analyzed by EDS in Fig. 5, which represents the atomic percentages of elements and Na/K ratios**

| Sample | | O | Na | K | Bi | Na/K | Ti |
|---|---|---|---|---|---|---|---|
| PLS | Matrix | 57.01 | 12.56 | 1.33 | 0.67 | 9.41 | 28.41 |
| | Rods | 66.78 | 5.43 | 3.03 | 0.06 | 1.78 | 24.67 |
| SF | Matrix | 40.87 | 7.67 | 6.32 | 3.07 | 1.21 | 42.04 |
| | Rods | 45.85 | 20.92 | 7.04 | 0.37 | 2.97 | 25.79 |
| SPS | Matrix | 77.87 | 1.32 | 0.47 | 13.42 | 2.8 | 6.91 |

### 3.4 Piezoresponse force microscopy

Figure 6 shows the amplitude and phase response as a function of applied DC bias voltage from –40 to +40 V at a drive frequency of 300 kHz applied between the tip and the bottom electrode. This causes the sample to vibrate at the same frequency due to the converse piezoelectric effect [32,33]. The amplitude (pm) versus voltage (V) exhibits the butterfly loops that describe the local displacement which are characteristic of the piezoelectric response in ferroelectric media. Figures 6(a), 6(d), and 6(g) depict such butterfly loops for the PLS, SF, and SPS samples that reveal the presence of expansion and contraction processes typical of ferroelectric domains. Meanwhile, Figs. 6(b), 6(e), and 6(h) illustrate the phase (°) versus voltage (V) plots that provides information about the local polarization switching behavior. The phase loops for PLS, SF, and SPS exhibit representative 180° polarization switching under voltage, which, in turn, establishes the presence of 180° domain walls. On the other hand, Figs. 6(c), 6(f), and 6(i) show the loops of the local piezoelectric coefficient ($d_{33}^*$) values as a function of voltage for PLS, SF, and SPS samples. Table 5 shows the PFM

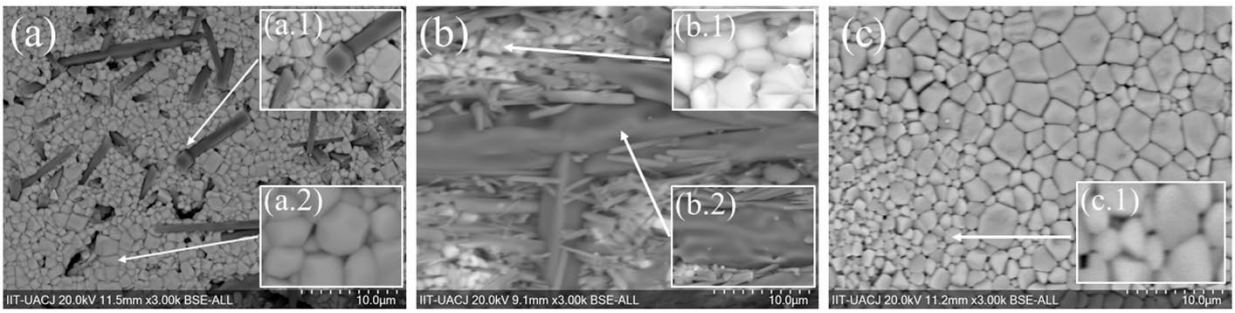


**Fig. 5** Regions where EDS analyses were performed on the PLS, SF, and SPS samples. EDS analysis results are shown in Table 4.

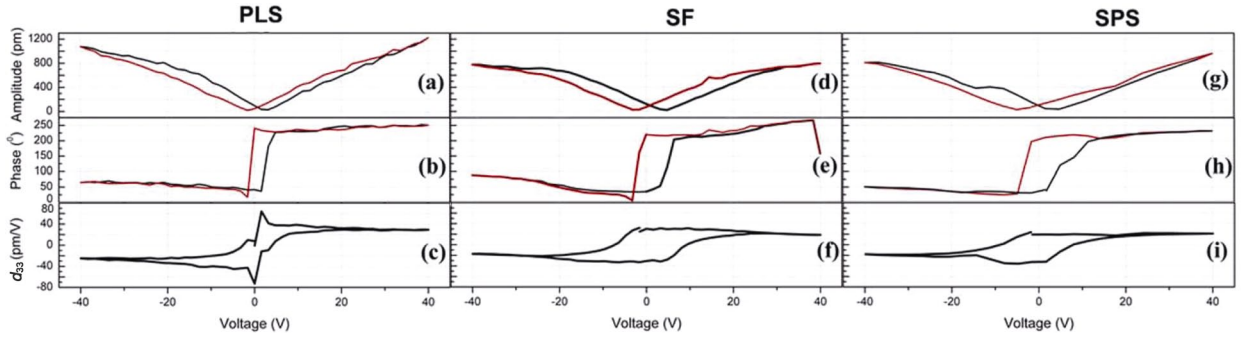


**Fig. 6** PFM analysis of the BNKT16 sintered ceramics by PLS, SF, and SPS: (a, d, g) PFM amplitude, (b, e, h) PFM phase, and (c, f, i) PFM local effective piezoresponse ($d_{33}$).

**Table 5 PFM parameter values obtained for the BNKT16 samples**

| Sample | $d_{33}^*$ at 40 V (pm/V) | Average crystallite size (nm) | $V_c$(V) |
|---|---|---|---|
| PLS | 64 | 146 | 1.63 |
| SF | 32 | 136 | 3.98 |
| SPS | 25 | 88 | 4.93 |

parameters values, $d_{33}^*$ at maximum voltage of 40 V, crystallite size, and the coercive voltage ($V_c$) obtained for the BNKT16 samples sintered by PLS, SF, and SPS. As can be appreciated, the $d_{33}^*$ and $V_c$ values are strongly influenced by the crystallite size. While the $d_{33}^*$ value decreases with the presence of smaller crystallite size. In the sequence of PLS, SF, and SPS, the $V_c$ values increase (Table 5). The lower piezoelectric coefficient of 25 pm/V coupled with the higher coercive voltage of 4.93 V for the SPS sample can be related to the lower crystallite size of 88 nm which promoted higher dispersion in the distributions of the domain walls [33].

### 3. 5 Electrical analysis

Figure 7 shows the global hysteresis loops, collected at room temperature, of the BNKT16 ceramic samples sintered by PLS, SF, and SPS. The hysteresis loops for the PLS (Fig. 7(a)) and SPS (Fig. 7(c)) are not in complete agreement with the PFM results previously discussed, where all samples exhibit similar and good local ferroelectric–piezoelectric properties. The elliptic shape and the inclination of the global loops in the Figs. 7(a) and 7(c), and the decrease of the polarization for the maximum value of the applied electric field, more pronounced for the SPS sample, can be associated with microstructural defects, spinning of domain walls, and dielectric loss due to electrical conduction along and across to the grain boundaries, among others. With this, the maximum ($P_{MAX}$) and remanent ($P_r$) polarization as well as the coercive electric field ($E_c$) are strongly affected and not reveal the real microscopic ferroelectric properties. Similarity in shape to the electric hysteresis loops of Figs. 7(a) and 7(c) for BNKT ceramic family has been previously reported [5]. However, the loops of the BNKT16 ceramic sample sintered by SF (Fig. 7(b)) exhibit a hysteresis behavior that looks closer to a hard ferroelectric material. In fact, the inflection point between remanent polarization and its corresponding coercive electric field can be clearly observed. SF

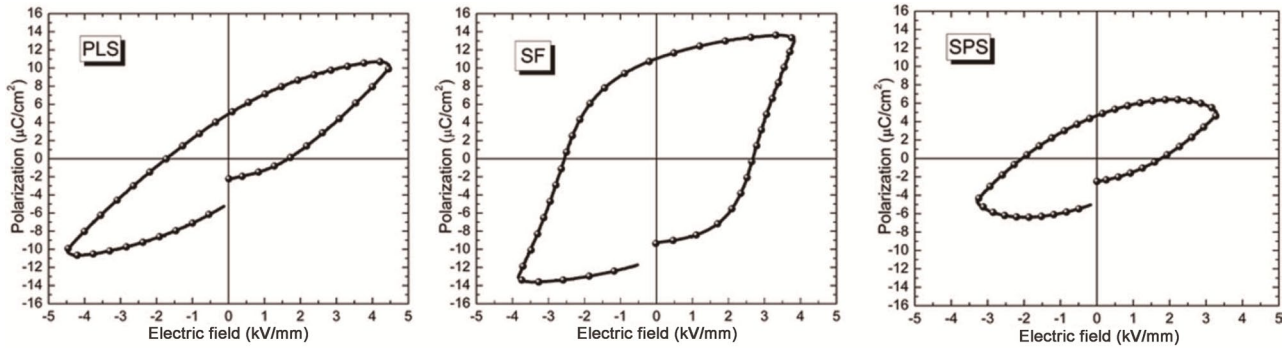


**Fig. 7** Hysteresis loops at room temperature of BNKT16 sintered ceramics of (a) PLS, (b) SF, and (c) SPS.

samples are the most compacted ones with the highest density.

Values of $d_{33}$, $P_r$, $E_c$, average grain sizes, and density of all ceramic samples are listed in Table 6. It can be observed that $d_{33}$, $P_r$, $E_c$ increase in the ordered sequence: SPS, PLS, and SF, which is the same order as the rhombohedral phase volume fraction increases (Table 1). It can also be noticed that grain size increases in the same sequence as well as the density (Table 6). SF samples have the largest grain size (1.89 μm) and thus the highest $d_{33}$ (165 pC/N) which is one of the top values reported in the literature [3,30]. The tendency in the grain size–piezoelectric propery relation of Table 6 has been reported in previous works [5,30] and is also observed herein. However, the BNKT composition has other important factors to consider and it is the presence of grains with different morphologies (Fig. 3) and different stoichiometric composition (Table 4).

The tendency of the observed properties in the sintered samples (Table 6) is associated with the morphology of SF specimen (Fig. 3(b)) that can be easily differentiated from PLS (Fig. 3(a)) and SPS (Fig. 3(c)) ones. For SF, the rod-like grains grow perpendicular to the direction of the uniaxial applied stress, and they are embedded in the gain matrix. The interaction between nearly spherical and rod-like grains, which can also be observed as a secondary phase, is expected to play a key role in the improvement of piezoelectric response as reported by Ramajo *et al*. [30] for their PLS sample. In the present work, this interaction is also presented for the PLS sample in lower amounts. For PLS sample, the volume fraction of rod-like grains is lower than the one of SF sample, and they are widely spread not showing a preferred orientation.

Crystallographic texture is expected to be another important factor that affects final piezoelectric properties. Table 7 reports the modified March's function $G_1$ parameter that describes the crystallographic texture (see FullProf_Manual). $G_1$ equal to 1.0 means no preferred orientation. When $G_1 < 1.0$, a crystallographic texture with platy habit type has been developed during sintering. The March–Dollase approach is commonly used to describe texture with the Rietveld method [34,35]. Hence, the lower the value between 0.0 and 1.0 for $G_1$, the formation of a crystallographic texture is more likely to occur. It can be observed from Table 7 that the texture for the PLS and SPS samples are quite similar and the SF experiments a remarkable higher texture. This result is congruent with the fact that a uniaxial stress applied during sintering favors the crystallographic orientation distribution along the stress direction. For the SPS sample, a stress is applied along the axial direction, but two facts need to be mentioned: SPS processing time is very short and the powders are confined inside a mold, then the stress applied along the axial sample direction produces a stress distribution [36]. As a result, not such a preferred orientation is developed like in the SF sample. Then, the stronger the texture, the higher the piezoelectric coefficient. Finally, it is worth to mention that for BNKT–*R*3*c* phase for the SF sample, a combination of three preferred orientations is found. It contributes to a better Rietveld refinement. SEM micrograph for SF (Fig. 4(b)) depictures a congruent statement with this Rietveld finding. For this microstructure, it can be expected that, at least, there exist two different preferred orientations, one for the nearly circular grains and the other one for the rod-like grains.

The highest piezoelectric coefficient globally measured is for SF sample. However, the PFM analysis reports that the highest piezoelectric response is for PLS sample. This does not have to be a contradicting result. The contributions for the piezoelectric coefficient can be found at different structural levels from the unit cell to the grain level. For example, SF sample can be described as a ceramic–ceramic composite whose nearly spherical grain matrix has well oriented rod-like

**Table 6 Ferroelectric and piezoelectric parameters, average grain size with its standard deviation, and densities of BNKT16 ceramic samples sintered by PLS, SF, and SPS**

| Sample | Ferroelectric parameter | | Piezoelectric coefficient $d_{33}$ (pC/N) | Grain size (μm) | Density (g/cm$^3$) |
|---|---|---|---|---|---|
| | $E_c$ (kV/mm) | $P_r$ (μC/cm$^2$) | | | |
| SF | 26.20 | 11.05 | 165 | 1.89 + 0.59 | 5.81 |
| PLS | 17.10 | 4.87 | 120 | 1.81 + 0.49 | 5.61 |
| SPS | 19.20 | 4.65 | 60 | 1.76 + 0.79 | 5.77 |

**Table 7 Modified March's function parameter $G_1$ to describe crystallographic texture**

| Sample–phase | Preferred direction | Fraction | $G_1$ |
|---|---|---|---|
| PLS–*R*3*c* | (101) | 1.0 | 0.7387 |
| SPS–*P*4*mm* | (101) | 1.0 | 0.7553 |
| | (101) | 0.5 | 0.6000 |
| SF–*R*3*c* | (001) | 0.2 | 0.6000 |
| | (110) | 0.3 | 0.6000 |

inclusions. In the line of this result, it is worth to mention that Ayrikyan *et al*. [37] reported that ceramic composites can be a way to increase the piezoelectric coefficient.

## 4 Conclusions

$Bi_{0.5}(Na_{0.84}K_{0.16})_{0.5}TiO_3$ (BNKT16) solid solution powders were synthesized by sol–gel. They were sintered by pressureless sintering (PLS), sinter forging (SF), and spark plasma sintering (SPS) techniques.

The coexistence of rhombohedral and tetragonal phases is observed for the sintered samples. The volume fraction of the rhombohedral phase increases following the sequence: SPS (2.56%), PLS (85.59%), and SF (97.52%). The largest crystallite size (146 nm) is found for PLS and the largest grain size (1.89 μm) for SF. Rod-like grains are detected for PLS and SF samples and they can be related to alkaline element volatilization, mainly Bi. The highest macroscopic piezoelectric coefficient is obtained for SF sample, and it is equal to 165 pC/N. SF sample shows the highest coercive field (26.20 kV/mm). Then, for BNKT ceramics, the increase in the rhombohedral phase, grain size, crystallographic texture, and crystallite size favor the piezoelectric coefficient. In addition, the appearance of a secondary phase improves the $d_{33}$ coefficient and even more if they pose a preferred orientation as observed for SF sample. Locally, at the nano-level, the highest piezoelectric response is obtained for PLS, whose crystallite size is higher than the ones of SF and SPS samples.

### Acknowledgements

The authors are indebted to CONACYT grant A1-S-9232 for their valuable support. GHC and JRLM are grateful to CONACYT for the Ph.D. scholarship.

### Electronic Supplementary Material

Supplementary material is available in the online version of this article at https://doi.org/10.1007/s40145-019-0314-8.

### References

[1] Quan ND, Bac HL, Thiet DV, *et al*. Current development in lead-free $Bi_{0.5}(Na,K)_{0.5}TiO_3$-based piezoelectric materials. *Adv Mater Sci Eng* 2014, **2014**: 365391.

[2] Rödel J, Jo W, Seifert KTP, *et al*. Perspective on the development of lead-free piezoceramics. *J Am Ceram Soc* 2009, **92**: 1153–1177.

[3] Camargo J, Ramajo L, Rubio-Marcos F, *et al*. Ferroelectric properties of $Bi_{0.5}(Na_{0.8}K_{0.2})_{0.5}TiO_3$ ceramics. *Adv Mater Res* 2014, **975**: 3–8.

[4] Chen P-Y, Chou C-C, Tseng T-Y, *et al*. Comparative study between conventional and microwave sintered lead-free BNKT ceramics. *Ferroelectrics* 2009, **381**: 196–200.

[5] Ullah A, Ahn CW, Hussain A, *et al*. The effects of sintering temperatures on dielectric, ferroelectric and electric field-induced strain of lead-free $Bi_{0.5}(Na_{0.78}K_{0.22})_{0.5}TiO_3$ piezoelectric ceramics synthesized by the sol–gel technique. *Curr Appl Phys* 2010, **10**: 1367–1371.

[6] Anjali K, Ajithkumar TG, Joy PA. Correlations between structure, microstructure, density and dielectric properties of the lead-free ferroelectrics $Bi_{0.5}(Na,K)_{0.5}TiO_3$. *J Adv Dielect* 2015, **5**: 1550028.

[7] Gonzalez AM, Pardo L, Montero-Cabrera ME, *et al*. Analysis of the rhombohedral–tetragonal symmetries coexistence in lead-free $0.94(Bi_{0.5}Na_{0.5})TiO_3$–$0.06BaTiO_3$ ceramics from nanopowders. *Adv Appl Ceram* 2016, **115**: 96–105.

[8] Liu X, Xue SD, Li F, *et al*. Giant electrostrain accompanying structural evolution in lead-free NBT-based piezoceramics. *J Mater Chem C* 2018, **6**: 814–822.

[9] Liu X, Li F, Li P, *et al*. Tuning the ferroelectric-relaxor transition temperature in NBT-based lead-free ceramics by Bi nonstoichiometry. *J Eur Ceram Soc* 2017, **37**: 4585–4595.

[10] Sasaki A, Chiba T, Mamiya Y, *et al*. Dielectric and piezoelectric properties of $(Bi_{0.5}Na_{0.5})TiO_3$–$(Bi_{0.5}K_{0.5})TiO_3$ systems. *Jpn J Appl Phys* 1999, **38**: 5564–5567.

[11] Li W, Xu ZJ, Chu RQ, *et al*. Synthesis and characterization of $(Na_{0.85}K_{0.15})_{0.5}Bi_{0.5}TiO_3$ ceramics by different methods. *Mater Res Bull* 2011, **46**: 871–874.

[12] Guilmeau E, Lambert S, Chateigner D, *et al*. Quantitative texture analysis of polyphased oxides by diffraction: Example of Bi2223 sinter-forged ceramic and Y123 foam superconductors. *Mat Sci Eng B* 2003, **104**: 107–112.

[13] Hao JJ, Wang XH, Chen RZ, *et al*. Preparation of textured bismuth titanate ceramics using spark plasma sintering. *J Am Ceram Soc* 2004, **87**: 1404–1406.

[14] Herrera Robles JO, Rodríguez González CA, de la Torre SD, *et al*. Dielectric properties of bismuth titanate densified by spark plasma sintering and pressureless sintering. *J Alloys Compd* 2012, **536**: S511–S515.

[15] Liu J, Shen ZJ, Nygren M, *et al*. SPS processing of bismuth-layer structured ferroelectric ceramics yielding highly textured microstructures. *J Eur Ceram Soc* 2006, **26**: 3233–3239.

[16] Kan YM, Wang PL, Xu T, *et al*. Spark plasma sintering of bismuth titanate ceramics. *J Am Ceram Soc* 2005, **88**:

1631–1633.

[17] Chen XM, Liao YW, Wang HP, *et al*. Phase structure and electric properties of $Bi_{0.5}(Na_{0.825}K_{0.175})_{0.5}TiO_3$ ceramics prepared by a sol–gel method. *J Alloys Compd* 2010, **493**: 368–371.

[18] Pérez-Mezcua D, Calzada ML, Bretos I, *et al*. Influence of excesses of volatile elements on structure and composition of solution derived lead-free $(Bi_{0.50}Na_{0.50})_{1-x}Ba_xTiO_3$ thin films. *J Eur Ceram Soc* 2016, **36**: 89–100.

[19] Rodríguez-Carvajal J. Recent advances in magnetic structure determination by neutron powder diffraction. *Phys B: Condens Matter* 1993, **192**: 55–69.

[20] Herrera-Pérez G, Castillo-Sandoval I, Solís-Canto O, *et al*. Local piezo-response for lead-free $Ba_{0.9}Ca_{0.1}Ti_{0.9}Zr_{0.1}O_3$ electro-ceramic by switching spectroscopy. *Mat Res* 2018, **21**: e20170605.

[21] Kreisel J, Glazer AM, Bouvier P, *et al*. High-pressure Raman study of a relaxor ferroelectric: The $Na_{0.5}Bi_{0.5}TiO_3$ perovskite. *Phys Rev B* 2001, **63**: 174106.

[22] Montero-Cabrera ME, Pardo L, García A, *et al*. The global and local symmetries of nanostructured ferroelectric relaxor $0.94(Bi_{0.5}Na_{0.5})TiO_3$–$0.06BaTiO_3$. *Ferroelectrics* 2014, **469**: 50–60.

[23] Jones GO, Thomas PA. Investigation of the structure and phase transitions in the novel A-site substituted distorted perovskite compound $Na_{0.5}Bi_{0.5}TiO_3$. *Acta Crystallogr Sect B* 2002, **58**: 168–178.

[24] Jones GO, Kreisel J, Thomas PA. A structural study of the $(Na_{1-x}K_x)_{0.5}Bi_{0.5}TiO_3$ perovskite series as a function of substitution ($x$) and temperature. *Powder Diffr* 2002, **17**: 301–319.

[25] Aroyo MI, Kirov A, Capillas C, *et al*. Bilbao crystallographic server. II. Representations of crystallographic point groups and space groups. *Acta Cryst Sect A* 2006, **62**: 115–128.

[26] Kroumova E, Aroyo MI, Perez-Mato JM, *et al*. Bilbao crystallographic server: Useful databases and tools for phase-transition studies. *Phase Transitions* 2003, **76**: 155–170.

[27] Wang J, Zhou Z, Xue J. Phase transition, ferroelectric behaviors and domain structures of $(Na_{1/2}Bi_{1/2})_{1-x}TiPb_xO_3$ thin films. *Acta Mater* 2006, **54**: 1691–1698.

[28] Prado-Espinosa A, Camargo J, del Campo A, *et al*. Exploring new methodologies for the identification of the morphotropic phase boundary region in the $(BiNa)TiO_3$–$BaTiO_3$ lead free piezoceramics: Confocal Raman microscopy. *J Alloys Compd* 2018, **739**: 799–805.

[29] Rout D, Moon KS, Rao VS, *et al*. Study of the morphotropic phase boundary in the lead-free $Na_{1/2}Bi_{1/2}TiO_3$–$BaTiO_3$ system by Raman spectroscopy. *J Ceram Soc Jpn* 2009, **117**: 797–800.

[30] Ramajo L, Camargo J, Rubio-Marcos F, *et al*. Influences of secondary phases on ferroelectric properties of $Bi(Na,K)TiO_3$ ceramics. *Ceram Int* 2015, **41**: 5380–5386.

[31] Ramajo L, Castro M, Rubio-Marcos F, *et al*. Influence of $MoO_3$ on electrical and microstructural properties of $(K_{0.44}Na_{0.52}Li_{0.04})(Nb_{0.86}Ta_{0.10}Sb_{0.04})O_3$. *J Mater Sci: Mater Electron* 2013, **24**: 3587–3593.

[32] Gruverman A, Kholkin A. Nanoscale ferroelectrics: Processing, characterization and future trends. *Rep Prog Phys* 2006, **69**: 2443–2474.

[33] Bharathi P, Thomas P, Varma KBR. Piezoelectric properties of individual nanocrystallites of $Ba_{0.85}Ca_{0.15}Zr_{0.1}Ti_{0.9}O_3$ obtained by oxalate precursor route. *J Mater Chem C* 2015, **3**: 4762–4770.

[34] Howard CJ, Kisi EH. Preferred orientation in Debye–Scherrer geometry: Interpretation of the March coefficient. *J Appl Cryst* 2000, **33**: 1434–1435.

[35] Zolotoyabko E. Fast quantitative analysis of strong uniaxial texture using a March–Dollase approach. *J Appl Cryst* 2013, **46**: 1877–1879.

[36] Camacho-Montes H, García-Casillas PE, Rodríguez-Ramos R, *et al*. Simulation of the stress-assisted densification behavior of a powder compact: Effect of constitutive laws. *J Am Ceram Soc* 2008, **91**: 836–845.

[37] Ayrikyan A, Prach O, Khansur NH, *et al*. Investigation of residual stress in lead-free BNT-based ceramic/ceramic composites. *Acta Mater* 2018, **148**: 432–441.